Inorganic Chemistry
Article
pubs.acs.org/IC

# $Al_3AuIr$: A New Compound in the Al–Au–Ir System

Joris Kadok,[†] Marie-Cécile de Weerd,[†] Pascal Boulet,[†] Émilie Gaudry,[†] Yuri Grin,[‡] Vincent Fournée,[†] and Julian Ledieu*,[†]

[†]Institut Jean Lamour (UMR7198 CNRS, Université de Lorraine), Parc de Saurupt, 54011 Nancy Cedex, France
[‡]Max-Planck-Institut für Chemische Physik fester Stoffe, Nöthnitzer Strasse 40, 01187 Dresden, Germany

**ABSTRACT:** A new ternary phase with a composition of $Al_3AuIr$ has been found in the Al-rich area of the Al–Au–Ir system. Differential thermal analysis indicates a melting point of 990 °C, and single-crystal X-ray diffraction measurements reveal that this ternary phase adopts a $Ni_2Al_3$ structure type (space group $P\bar{3}m1$) with $a$ = 4.2584(5) Å and $c$ = 5.1991(7) Å. This compound is isostructural to the $Al_3Cu_{1.5}Co_{0.5}$ phase also found in the Al-rich part of the Al–Cu–Co ternary diagram. Experimental evidence combined with ab initio calculations point toward an $Al_3AuIr$ phase stabilized by a Hume–Rothery mechanism. Quantum chemical calculations indicate two-center and multicenter interactions in the $Al_3AuIr$ phase. Layered distribution of two-center interactions separated by regions with four- and five-center bonds suggests a preferential cleavage of the material at puckered planes perpendicular to the [001] direction.

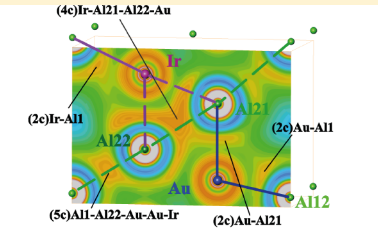

Chemical bonding for the $Al_3AuIr$ compound

## 1. INTRODUCTION

Within a given ternary system, substituting transition metals (TMs) by elements of the same column in the Periodic Table can lead to compounds that share similar physical and chemical properties. This was demonstrated by Tsai et al., who found stable icosahedral quasicrystals by replacing Fe with either Ru or Os in Al–Cu–Fe,[1] hence suggesting that Al-based quasicrystals are electronically stabilized (Hume–Rothery phases). For the Al–Ir–TM system, several stable quasicrystalline or approximant phases have also been discovered. For instance, a decagonal quasicrystal with a nominal composition of $Al_{73}Ir_{14.5}Os_{12.5}$ has been reported in the Al-rich part of the Al–Ir–Os phase diagram.[2] Its structure along the 10-fold axis can be described as a periodic stacking of eight quasiperiodic layers of atoms, leading to a 16.8 Å periodicity.[2] Similarly, stable decagonal $Al_{65}Ir_{15}Cu_{25}$[3] (for other compositions, see refs 4 and 5) and icosahedral $Al_{60}Ir_{20}Cu_{20}$ phases[3] and recently a cluster-based cubic phase with a composition of $Al_{63.3}Ir_{24.4}Cu_{12.3}$[5] have been identified in the Al–Ir–Cu system. The structure of the $Al_{63.3}Ir_{24.4}Cu_{12.3}$ intermetallic compound consists of a packing of endohedral clusters. The latter is considered as a (2 × 2 × 2)-fold superstructure of a 1/0 approximant of a Mackay-cluster-based icosahedral quasicrystal.[5] This type of structure (comparable unit cell dimensions and space group) has also been observed in a $Al_{64.5}Ir_{13.5}Pd_{22}$ sample,[6] although the latter structure remains to be fully determined. As explained above, complex intermetallic phases exist in the Al–Ir–(Os, Cu, Pd) systems. With the aim of finding new compounds, we have replaced Cu by Au in the Al–Ir–Cu system and have explored the Al–Au–Ir ternary system, starting with a composition similar to what has already been selected in previous studies, i.e., in the Al-rich part of the phase diagram (65–70 atom % Al).[2–6] Several binary phases have already been reported in the Al–Ir and Al–Au systems including the following ones: AlAu, $AlAu_4$, $Al_2Au$, $AlAu_2$, $Al_3Au_8$, and $Al_2Au_3$[7] and $Al_9Ir_2$, $Al_{45}Ir_{13}$, $Al_{13}Ir_4$, $Al_{28}Ir_9$, $Al_3Ir$, $Al_{2.7}Ir$, and AlIr.[8] Au–Ir near-surface alloys have been considered in the Au/Ir(111) system[9] to explain the anomalous hydrogen interaction with Au monolayers.[10] In the following, we report the existence of a new ternary phase, and we determine its crystallographic structure.

## 2. EXPERIMENTAL AND CALCULATION DETAILS

**2.1. Experimental Details.** One ingot weighing 0.5 g with a nominal composition of $Al_{65}Au_{20}Ir_{15}$ was synthesized from high-purity Al, Au, and Ir metals. The sample was prepared by arc melting under a partial argon atmosphere. For homogenization, it was turned over and remelted several times. A thin black powder was found deposited on the hearth pad after the melting. Powder X-ray diffraction (XRD) revealed this to be pure Al, hence explaining the mass loss of about 2% that the sample underwent. The ingot was then wrapped in Ta foil, sealed in an evacuated quartz tube filled with a partial $He/H_2$ 10% atmosphere, and annealed to 950 °C for 72 h. A small fraction of the sample was found evaporated on the Ta foil after the annealing treatment. The as-cast and annealed samples were studied by standard metallographic techniques, powder XRD (using Cu $K\alpha_1$ radiation), optical microscopy, and scanning electron microscopy (SEM). The local phase compositions were obtained by SEM with energy-dispersive X-ray analysis (EDX), and the melting points of the different phases were determined using differential thermal analysis (DTA) with heating and cooling rates of 10 °C $min^{-1}$. Single crystals were obtained from a crushed part of a sample. The XRD data were collected on a Bruker Kappa Apex II diffractometer equipped with a mirror monochromator and a Mo $K\alpha$ IμS ($\lambda$ = 0.71073 Å). The *Apex 2* program package was used for the cell refinements and data reductions. The structure was solved by using direct methods and refined with the *SHELXL-2013*[11] and *WinCSD*[12] programs. Semi-empirical absorption correction (*SADABS*) was applied to the data.

**2.2. Structural Relaxations.** Electronic structure calculations and structural relaxations were performed for the three ordered models

**Received:** April 30, 2015
**Published:** August 4, 2015

DOI: 10.1021/acs.inorgchem.5b00946
*Inorg. Chem.* 2015, 54, 7898–7905

### Table 1. Crystallographic Data for $Al_3AuIr$

| | |
|---|---|
| chemical formula | $Al_3AuIr$ |
| formula weight (g $mol^{-1}$) | 470.11 |
| temperature (K) | 296(2) |
| wavelengh (Å) | 0.71073 |
| cryst size ($\mu$m) | 22 × 22 × 22 |
| cryst syst | trigonal |
| space group | $P\bar{3}m1$ (No. 164) |
| unit cell dimens (Å) (hexagonal setting) | $a = 4.2584(5)$, $c = 5.1991(7)$ |
| volume ($Å^3$) | 81.65(2) |
| $Z$ | 1 |
| calcd density (g $cm^{-3}$) | 9.561 |
| abs coeff ($mm^{-1}$) | 86.084 |
| $F(000)$ | 195 |
| $\theta$ range for data collection (deg) | 3.92−35.60 |
| index ranges | $-6 \leq h \leq 5$, $-6 \leq k \leq 6$, $-8 \leq l \leq 8$ |
| collected, indep reflns | 1377, 161 |
| coverage of the reciprocal sphere (%) | 95.3 |
| GOF | 1.323 |
| $R$ indices | $R$(int) = 0.0495, R1 = 0.0177, wR2 = 0.0397 |
| extinction coeff | 0.130(8) |
| no. of param refined | 10 |
| $\Delta\rho_{max}$, $\Delta\rho_{min}$ (e $Å^{-3}$) | 2.78, −2.62 |

### Table 2. Atomic Coordinates and Isotropic Displacement Parameters for $Al_3AuIr$ (Ideal Model)

| atom | site | $x$ | $y$ | $z$ | $U_{eq}$ ($Å^2$) | occupancy |
|---|---|---|---|---|---|---|
| Al1 | 1a | 0 | 0 | 0 | 0.033(2) | 1 |
| Al2 | 2d | $^1/_3$ | $^2/_3$ | 0.6459(7) | 0.0133(8) | 1 |
| Au1/Ir1 | 2d | $^1/_3$ | $^2/_3$ | 0.16360(6) | 0.00677(17) | 0.5/0.5 |

$Al_3AuIr$, $Al_6Au_3Ir$, and $Al_6AuIr_3$. The $Al_3AuIr$ crystal structure was built using the cell parameters of Table 1 and the atomic positions of Table 2 with one Ir atom in one of the two 2d sites ($^1/_3$, $^2/_3$, 0.1636) and one Au atom in the other one ($^2/_3$, $^1/_3$, −0.1636). The crystal structures of $Al_6Au_3Ir$ and $Al_6AuIr_3$ were built by doubling the periodicity along the $c$ axis. The resulting cells contain then four TM atoms: three Au (respectively three Ir) and one Ir (respectively one Au) atoms in the case of the $Al_6Au_3Ir$ (respectively $Al_6AuIr_3$) phase.

The VASP package[13−16] was used for calculations based on the density functional theory (DFT). VASP performs a variational solution of the Kohn−Sham equations in a plane-wave basis. We used the projector-augmented wave method[17,18] and the generalized gradient approximation of Perdew−Burke−Ernzerhof[19,20] to describe the interactions. The following cutoff and $k$-points grid were used for the calculations ($Al_3AuIr$ model): $E_{cut} = 500$ eV; 29 × 29 × 13 $k$-points grid. The calculation of the Hellmann−Feynman forces on the atoms allows us to perform a full optimization of the atomic positions in the unit cell and of the lattice parameters. The total energies and density of states (DOS) were calculated using the relaxed structures. The formation enthalpies are given with reference to pure Al, Au, and Ir (a face-centered-cubic system).

**2.3. Analysis of the Chemical Bonding.** Analysis of the chemical bonding was performed for the ordered $Al_3AuIr$ model using the lattice parameters and atomic coordinates from the crystal structure refinement of single-crystal XRD data (see Tables 1−4) and changing of the occupation of the TM position. These criteria chosen to generate the $Al_3AuIr$ model led locally to a completely ordered structure. For $Al_3AuIr$, the symmetry was reduced from $P\bar{3}m1$ to $P3m1$. The $z$ coordinates for the two, in this space group independent, atoms Al21 and Al22 representing the Al2 position in the structure refinement were fixed at values reflecting their positions in the experimental structure. So, the calculations were performed for different positions of Al1 with $z$ = 0.0 (Al11), 0.063, and −0.063 (Al12). The *TB-LMTO-ASA* program package[21] was employed using the von Barth−Hedin exchange potential[22] for the local-density approximation calculations. The radial scalar-relativistic Dirac equation was solved to obtain the partial waves.[23] The addition of empty spheres was not necessary because the calculation within the atomic sphere approximation (ASA) includes corrections for the neglect of interstitial regions and partial waves of higher order.[24] The following radii of the atomic spheres were applied for calculations on $Al_3AuIr$: $r$(Ir) = 1.638 Å, $r$(Au) = 1.593 Å, $r$(Al1) = 1.606 Å, $r$(Al21) = 1.530 Å, and $r$(Al22) = 1.489 Å. A basis set containing Au(6s,6p,5d), Ir(6s,6p,5d), and Al(3s,3p) orbitals was employed, with Au(5f), Ir(5f), and Al(3d) functions being downfolded.

The electron localizability indicator (ELI, Υ) was evaluated in the ELI-D (distribution of the ELI) representation[25−27] with an ELI-D module within the *TB-LMTO-ASA* program package. Estimation of the shapes, volumes, and charges of the atoms after Bader (quantum theory of atoms in molecules, QTAIM[26]) and topological analysis of the ELI, e.g., localization of the ELI maxima as indicators of the direct atomic interactions, estimation of their basins, as well as calculations of the QTAIM/ELI-D intersections,[27] were performed with the program *DGrid*.[28]

### Table 3. Anisotropic Atomic Displacement Parameters ($Å^2$) for $Al_3AuIr$ (Ideal Model)

| atom | $U_{11}$ | $U_{22}$ | $U_{33}$ | $U_{12}$ | $U_{13}$ | $U_{23}$ |
|---|---|---|---|---|---|---|
| Al1 | 0.0085(15) | $U_{11}$ | 0.082(7) | 0.0042(7) | 0 | 0 |
| Al2 | 0.0161(12) | $U_{11}$ | 0.0075(15) | 0.0081(6) | 0 | 0 |
| Au1/Ir1 | 0.00765(19) | $U_{11}$ | 0.0050(2) | 0.00383(9) | 0 | 0 |

### Table 4. Atomic Coordinates and Isotropic Displacement Parameters for $Al_3AuIr$ (Split Model)

| atom | site | $x$ | $y$ | $z$ | $U_{eq}$ ($Å^2$) | occupancy |
|---|---|---|---|---|---|---|
| Al11 | 1a | 0 | 0 | 0 | 0.0122(8) | 0.5 |
| Al12 | 2c | 0 | 0 | 0.062(4) | 0.0119(8) | 0.25 |
| Al2 | 2d | $^1/_3$ | $^2/_3$ | 0.645(1) | 0.0167(12) | 1 |
| Au1/Ir1 | 2d | $^1/_3$ | $^2/_3$ | 0.16357(9) | 0.0091(2) | 0.5/0.5 |

## 3. RESULTS AND DISCUSSION

**3.1. Composition and Thermal Behavior.** Figure 1 exhibits typical optical microscopy images collected on polished as-cast and annealed samples. For the as-cast sample shown in

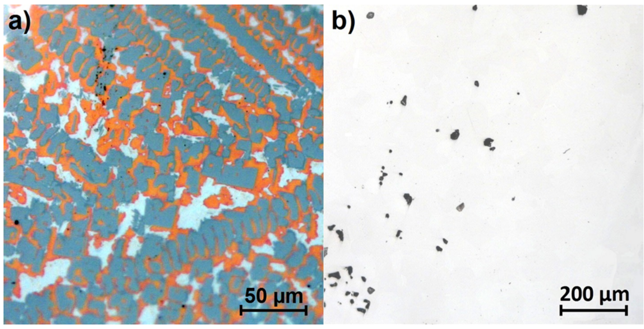

**Figure 1.** Optical microscopy images of the (a) as-cast and (b) annealed $Al_{65}Au_{20}Ir_{15}$ samples. (a) The black (gray) regions mark the $Al_{2.7}Ir$ phase, the gray (orange) represents the $Al_2Au$ phase, and the bright (almost white) area corresponds to the ternary alloy. (b) Only the ternary phase is observed, and the black areas are pores.

Figure 1a, three phases have been identified. They are referred to as the black, gray, and bright phases, appearing gray, orange, and nearly white in true color, respectively. Prior to polishing the sample, the black phase can be described by a distribution of well-faceted cubes (edge length ≤50 μm) surrounded by the gray and bright phases. The black phase seems to have solidified first, followed by the other two phases that would have solidified simultaneously. The EDX measurements have revealed the black phase to be $Al_{2.7}Ir$, the gray one to be $Al_2Au$, and the bright one to be a Al−Au−Ir ternary phase. Although the $Al_2Au$ compound has a orange/reddish tint here (similar color to that in ref 29), it is a well-known phase referred to as the "purple plague" in integrated electronics.[30] From optical microscopy observations (see Figure 1b), the annealed sample appears to be almost entirely single-phase with the presence of porosities. This ternary phase can have slightly different color contrasts, and extensive EDX measurements revealed different compositions ranging from $Al_{56}Au_{23}Ir_{21}$ to $Al_{64}Au_{18}Ir_{18}$, indicating a certain homogeneity range. Some material evaporation, which is inherent to the arc-melting technique, has occurred during the specimen preparation.

The XRD patterns of the as-cast and annealed samples are depicted in Figure 2. The diffractogram of the as-cast sample in Figure 2a is indexed using the two well-known $Al_2Au$[31] and $Al_{2.7}Ir$ phases[32] as impurities. The material for XRD measurements of the annealed sample has been taken from a homogeneous region. The annealed sample diffractogram in Figure 2b displays sharp and intense peaks, indicative of large crystallites. The peaks present on this diffractogram correspond to those not indexed in Figure 2a. They are associated with the peaks of the ternary phase revealed by EDX.

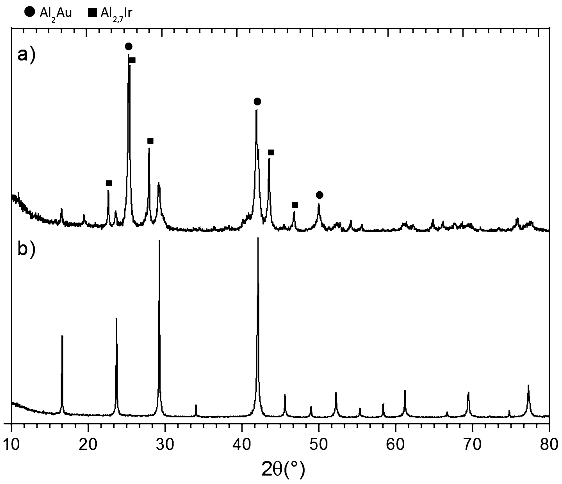

**Figure 2.** Powder XRD patterns of the (a) as-cast and (b) annealed samples.

DTA analysis was carried out on the as-cast sample between 600 and 1200 °C (with heating and cooling rates of 10 °C $min^{-1}$). The DTA curve in this region (see Figure 3) seems to bear at least two thermal effects: decomposition of the $Al_2Au$ phase (known to take place at 1060 °C[33]) and decomposition of the ternary phase at 990 °C. This would explain the appearance of the single crystals used hereafter. Because of the temperature range used, the feature associated with the decomposition of the $Al_{2.7}Ir$ phase could not be observed because it occurs around 1640 °C.[34] These values are consistent with the optical microscopy observations regarding the order of the solidification of the different phases.

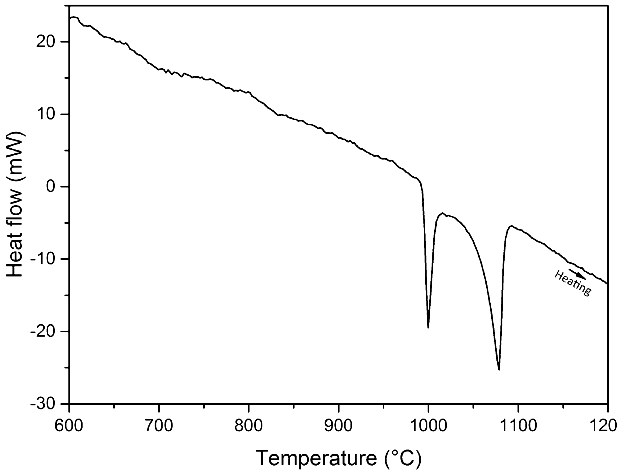

**Figure 3.** DTA heating curve (10 °C $min^{-1}$) of the three-phase as-cast sample.

**3.2. Crystal Structure.** A single crystal was obtained from a single-phase region of the annealed sample and was analyzed by single-crystal XRD using the Mo $K\alpha_1$ radiation. Reconstructed sections of the reciprocal space are not included because no additional information could be gained from the different planes measured. The final trigonal unit cell parameters are $a$ = 4.2584(5) Å and $c$ = 5.1991(7) Å, and the crystal structure was successfully solved in the centrosymmetric space group $P\bar{3}m1$. The three atomic positions have been obtained by direct methods. This ternary phase has a total composition of $Al_3AuIr$ and corresponds to the $Ni_2Al_3$ structure type (see Figure 4a). The EDX measurements performed on the same single crystal indicate equal content of Ir and Au within the accuracy of the measurements ($Al_{59}Ir_{19.5}Au_{21.5}$). This results in the occupation of one atomic position 2d by a mixture of Au−Ir (respectively 0.5/0.5). To validate the composition measured by EDX, the structure refinement has been performed on the fractional occupancy of the 2d position of the Au/Ir site. The results did not lead to significant changes or to improvement of the reliability factor. The complete crystallographic data are available in Table 1, the atomic coordinates and isotropic displacement parameters for this ideal model are shown in Table 2, and the anisotropic displacement parameters are given in Table 3.

**3.3. Split Model.** In order to understand the unusually strong displacement anisotropy of the Al1 position calculated with $z$ = 0 (hereafter Al11), the difference density map was calculated without any atoms at this place. The so-obtained difference density distribution reveals marked elongation in the [001] direction (Figure 5, top). Such a distribution cannot be described completely either by locating Al atoms in the off-center position (the coordinate $z$ = 0.063 resulted from the final refinement) with an isotropic displacement parameter ($u$ = 0.0119, Al12 position) or by positioning the Al in the ideal position with $z$ = 0.0 (Al11 position). In both cases, a nonnegligible part of the density remains undescribed (Figure 5, middle panel). Only after location of Al in equal amounts in both positions does the final difference electron density map show only very weak features in the vicinity of the Al1 position (Figure 5, bottom). The results of the final refinement are shown in Tables 1, 4, and 5; the interatomic distances are listed

DOI: 10.1021/acs.inorgchem.5b00946
Inorg. Chem. 2015, 54, 7898−7905

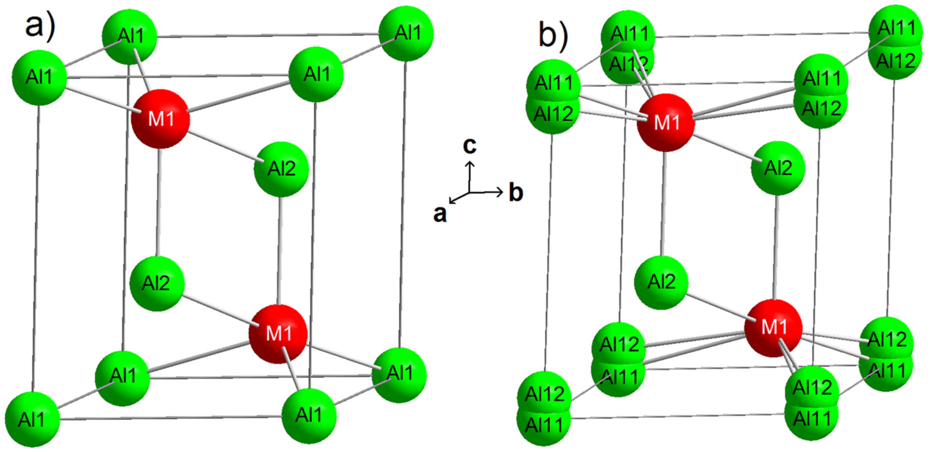

**Figure 4.** (a) Unit cell of $Al_3AuIr$, where M1 is either a Au or a Ir atom (ideal model: space group $P\bar{3}m1$). (b) Representation of the split model.

in Table 6. The appearance of Al in different positions in this part of the crystal structure (see Figure 4b) correlates with the locally different coordination of this site by Ir and Au atoms having different sizes. In the case of a symmetrical environment (with either Ir or Au coordinating this position), Al occupies the Al11 position, and in the case of a nonsymmetrical environment (Ir and Au in equal amounts coordinate Al1), the Al12 atoms are shifted from the ideal position at $z = 0.0$. The intermediate variants of occupation may cause smaller shifts.

The DFT structural relaxations obtained on $Al_3AuIr$ are consistent with the cell parameters deduced from XRD analysis ($a = 4.28$ Å and $c = 5.26$ Å) and with the atomic displacement proposed in the split model. For the noncentrosymmetric $Al_3AuIr$ structure, a displacement of Al1 atoms by $z = 0.069$ is observed, while the mean positions of the Al2 and TM atoms remain roughly unchanged ($z^{\mathrm{mean}}_{\mathrm{Al2}} = 0.647$ and $z^{\mathrm{mean}}_{\mathrm{TM}} = 0.166$). To investigate how the interatomic distances evolve with the TM decoration inside the structure, the fictitious $Al_6Au_3Ir$ and $Al_6AuIr_3$ compounds have been considered. They are built by doubling the periodicity along the $c$ axis. The Al1−Au distance $d^{\mathrm{Au,Ir}}_{\mathrm{Al1-Au}}$ is increased in a mixed environment (Au and Ir) compared to the one ($d^{\mathrm{Au}}_{\mathrm{Al1-Au}}$) obtained in a Au-rich environment ($d^{\mathrm{Au,Ir}}_{\mathrm{Al1-Au}} - {}^{\mathrm{Au}}_{\mathrm{Al1-Au}} \simeq 0.30$ Å). In the same way, the Al1−Ir distance $d^{\mathrm{Au,Ir}}_{\mathrm{Al1-Ir}}$ in a mixed environment is smaller than the one ($d^{\mathrm{Ir}}_{\mathrm{Al1-Ir}}$) found in an Ir-rich environment ($d^{\mathrm{Ir}}_{\mathrm{Al1-Ir}} - {}^{\mathrm{Au,Ir}}_{\mathrm{Al1-Ir}} \simeq 0.22$ Å). These observations are consistent with the results presented in section 3.4 based on the ELI approach.

The structure of this new compound $Al_3AuIr$ belongs to the structure type $Ni_2Al_3$[35] and is related to that of the $Al_3Cu_{1.5}Co_{0.5}$ phase, a compound crystallizing in the same trigonal crystal system (space group $P\bar{3}m1$) with parameters close to the here-reported ternary alloy: $a = 4.116$ Å and $b = 4.938$ Å.[36,37] The close relationship between these two phases may be explained by the replacement of Co and Cu with Ir and Au atoms, elements of the same group in the Periodic Table. The $Al_3Cu_{1.5}Co_{0.5}$ phase has a nominal composition ($Al_{60}Cu_{30}Co_{10}$) slightly different from that of the new ternary alloy $Al_{60}Au_{20}Ir_{20}$ (richer in elements of the VIII−B group). According to Grushko et al.,[37] the $Al_3Cu_{1.5}Co_{0.5}$ phase exists in a quite wide region, between 58 and 62 atom % Al and 12−20 atom % Co. However, electronic structure calculations using the tight-binding linear muffin-tin orbital method performed by Sabiryanov et al.[38] concluded that the $Al_{60}Cu_{30}Co_{10}$ phase is thermodynamically stable while the $Al_{60}Cu_{20}Co_{20}$ phase is not. The cohesive energy of the $Al_3Cu_{1.5}Co_{0.5}$ compound is found to be slightly larger than that of the $Al_3CuCo$ compound. The calculated electronic DOS exhibits a small minimum (pseudogap) at the Fermi level in the case of the $Al_3Cu_{1.5}Co_{0.5}$ compound but not for the $Al_{60}Cu_{20}Co_{20}$ phase. Authors concluded that the latter is not stabilized by a Hume−Rothery mechanism, while the Fermi surface−Brillouin zone interaction contributes to stabilization of the former.[38]

In the present study, it appears that a Au to Ir ratio equal to 1 is favorable in the Al−Au−Ir system, and it results in a stable phase. We note that the $Al_3Ni_2$ structure type (space group $P\bar{3}m1$) is common to $Al_3Pd_2$ and $Al_3Pt_2$, i.e., for all TM elements of the same column of the Periodic Table.[39,40] Therefore, the formation of stable $Al_3TM_2$ compounds (with TM = Ni, Pd, or Pt) is equivalent to an isoelectronic substitution because elements of the same column have similar chemistry. The formation of the $Al_3AuIr$ compound can also be viewed as an isoelectronic substitution of Pt atoms, with adjacent TM elements Ir and Au having similar Pauling electronegativities. This strongly suggests a Hume−Rothery stabilization mechanism for the $Al_3AuIr$ phase, contrary to the $Al_3CuCo$ case. This mechanism is based on a Fermi sphere−Brillouin zone interaction, where a reduction of the DOS at the Fermi level contributes to stabilization of the crystal (for a review, see refs 41 and 42). The electronic DOSs of the three $Al_3TM_2$ phases (TM = Ni, Pd, or Pt) have been calculated using a full potential linear muffin-tin orbital method. In each case, a marked pseudogap at the Fermi level is observed in agreement with the Hume−Rothery picture.[43,44] We can further estimate if the Hume−Rothery condition $2k_F = K_{hkl}$ is satisfied for some intense Bragg reflections. Assuming a negative valence of −0.6 for the (Au, Ir) pair inferred from Raynor's value for Ni and a valence of 3+ for Al, the Fermi wave vector is approximated using a free electron model, which leads to $2k_F = 2.8$ Å$^{-1}$, a value close to that of the $K_{110}$, $K_{102}$, and $K_{012}$ Bragg planes (2.95 Å$^{-1}$) associated with the most intense diffraction peak in Figure 2b. This again suggests a Hume−Rothery stabilization mechanism.

## 3.4. Electronic Structure and Chemical Bonding.

To confirm this hypothesis, ab initio calculations have been performed. Figure 6 presents the electronic DOSs calculated for the $Al_6Au_3Ir$, $Al_6AuIr_3$, and $Al_3AuIr$ phases. The DOSs of both $Al_6Au_3Ir$ and $Al_3AuIr$ systems show a broad local minimum in the vicinity of the Fermi level. The overall shape of the $Al_3AuIr$ DOS is similar to that of the $Al_3Pt_2$ system.[43,44] In addition, $E_F$ is located within a broad minimum of the DOS.

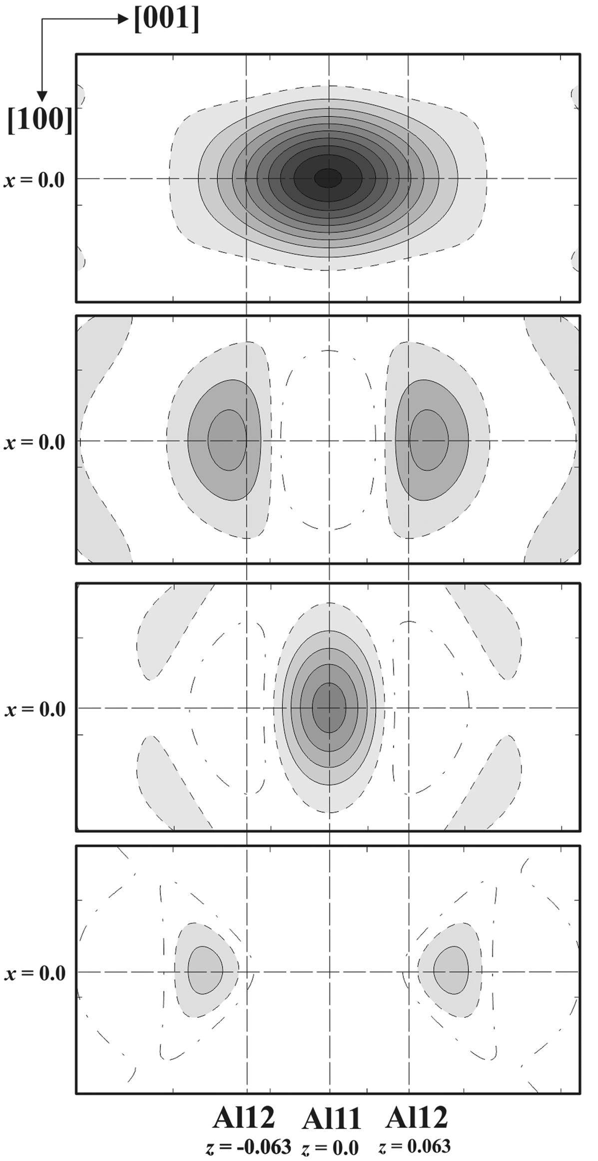

**Figure 5.** Distribution of the difference electron density in the (010) plane in the vicinity of the Al1 position: (top panel) calculated without any atoms in the Al1 position; (upper middle panel) calculated with Al in the Al12 position; (lower middle panel) calculated with Al in the Al11 position; (bottom panel) calculated with Al in equal amounts in the Al11 and Al12 positions. In the upper three panels, the isolines are drawn with a step of 4 e Å$^{-3}$, and in the bottom panel, with a step of 0.4 e Å$^{-3}$. Positive values of the difference density are shown with solid lines, zero values with dashed lines, and negative values with dash-dotted lines. The scale ticks on the axes are shown with a step of 0.5 Å.

**Table 5. Anisotropic Atomic Displacement Parameters (Å$^2$) for $Al_3AuIr$ (Split Model)**

| atom | $U_{11}$ | $U_{22}$ | $U_{33}$ | $U_{12}$ | $U_{13}$ | $U_{23}$ |
|---|---|---|---|---|---|---|
| Al2 | 0.017(2) | $U_{11}$ | 0.010(2) | 0.0086(8) | 0 | 0 |
| Au1/Ir1 | 0.0089(3) | $U_{11}$ | 0.0067(3) | 0.0044(1) | 0 | 0 |

**Table 6. Main Interatomic Distances (Å) for $Al_3AuIr$**

| atom | distance |
|---|---|
| Au1/Ir1−6Al11 | 2.6015(3) |
| Au1/Ir1−3Al12 | 2.514(4) |
| Au1/Ir1−3Al12 | 2.726(8) |
| Au1/Ir1−Al2 | 2.507(5) |
| Au1/Ir1−3Al2 | 2.651(2) |
| Au1/Ir1−Al2 | 2.692(5) |
| Au1/Ir1−3Au1/Ir1 | 2.9896(5) |
| Al12−Al12 | 0.65(3) |
| Al2−6Al11 | 3.072(3) |
| Al2−3Al12 | 2.888(10) |
| Al2−3Al12 | 3.277(13) |
| Al2−3Al2 | 2.889(4) |

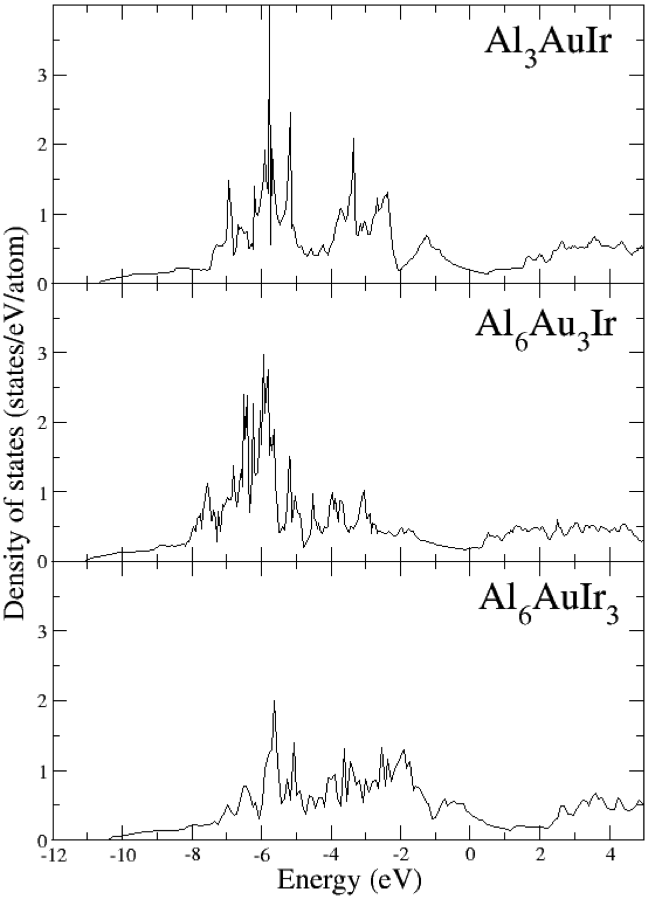

**Figure 6.** Electronic DOSs calculated for the $Al_6Au_3Ir$ (top) and $Al_3AuIr$ (bottom) models. The Fermi level is located at $E$= 0 eV.

To analyze the stability of the Al−Au−Ir phases, total energy calculations have been carried out and lead to a formation enthalpy of −0.681 eV atom$^{-1}$ for the $Al_3AuIr$ compound, while it is −0.517 and −0.730 eV atom$^{-1}$ for the $Al_6Au_3Ir$ and $Al_6AuIr_3$ compounds, respectively. These results clearly demonstrate a higher stability of the $Al_3AuIr$ phase compared to the $Al_6Au_3Ir$ composition, i.e., consistent with the absence of the $Al_6Au_3Ir$ phase in the samples characterized. Contrary to the Al−Cu−Co system, here a Au to Ir ratio equal to 1 is favored. As demonstrated by the $Al_6AuIr_3$ compound, other chemical variants may lead to more favorable formation enthalpies. Here, the formation enthalpy of −0.730 eV atom$^{-1}$ obtained for the $Al_6AuIr_3$ compound would suggest at first an even higher stability. However, this hypothetical composition has not been observed experimentally and has been considered only to complete our systematic approach. Hence, it is suggested that a configurational entropy contribution (higher for the 1:1 than for the 1:3 Au/Ir ratio) may counterbalance the formation enthalpy difference of 49

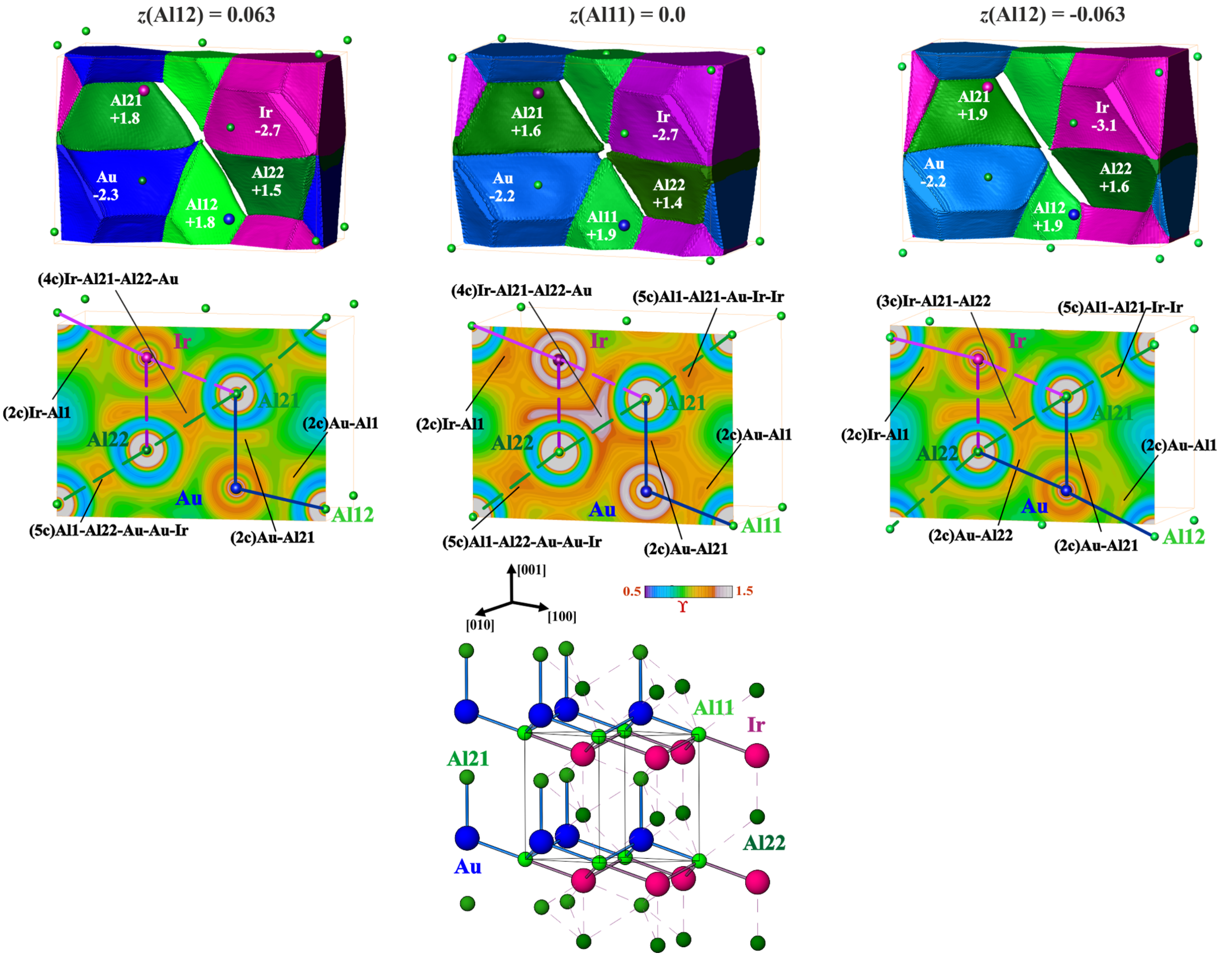

Figure 7. Chemical bonding in three models of $Al_3AuIr$ with different positions of the Al1 atoms: (top) shapes and effective charges of the QTAIM atoms; (middle) ELI-D in the (110) plane with assignment of the ELI-D attractors to the two-center and multicenter interactions according to the intersection technique; (bottom) distribution of the two-center and multicenter bonds in the ordered model of $Al_3IrAu$. Two-center interactions are shown with solid lines, and multicenter ones are represented with dashed lines.

meV atom$^{-1}$ between both phases, then resulting in a greater stability of the $Al_3AuIr$ phase.

To gain further insight into the bonding present within the Al−Au−Ir compound, quantum chemical calculations have been performed for the $Al_3AuIr$ composition. For this ternary model, the noncentrosymmetric space group $P3m1$ was used with three different values for the $z$ coordinate of the Al1 position. The lowest total energy was calculated for the ordered $Al_3AuIr$ structure with Al at the Al12 site and $z = -0.063$, being slightly larger for $z = 0.0$ and the largest one for $z = 0.063$. The Au/Ir distribution is presented in Figure 7. This model is in well-agreement with the atomic radii of Au and Ir (1.44 and 1.35 Å, respectively), showing longer Au−Al12 distances compared to the Ir−Al12 ones.

The shapes and effective charges of the QTAIM atoms (Figure 7, top) are in well-agreement with the electronegativity values of the components. Au and Ir show negative effective charges playing the role of electron acceptors but revealing different charges independently on the position of Al1. Al atoms show different positive charges depending on their environment. The lower difference between the charges of different Al atoms is observed with Al1 in the off-center position Al12. For the Al12 position, the lowest difference between Au and Ir effective charges is observed for $z = 0.063$, thus revealing this model as one with the most regular distributions of atomic charges. In general, taking into account large effective charges, charge transfer makes a large contribution to stabilization of the structural pattern of $Al_3IrAu$.

The ELI-D in the vicinity of the atom nuclei in $Al_3AuIr$ reveals strong deviations from the spherical shape characteristic for the isolated atoms (Figure 7, middle). The deviations are stronger in the valence region (i.e., in the last atomic shells), but also the penultimate shells of Ir and Au show clear nonsphericity, indicating participation of the electrons of these shells in the bonding interactions.[45,46] Independently of the $z$ coordinate for Al1, there are six different types of ELI-D maxima (attractors) in the unit cell. Their functions in the bonding pattern are different depending on the value of $z$(Al1). For the model with $z = 0.0$, the three symmetrically equivalent ELI-D attractors around each Au−Al21 contact reflect well the ring attractor of the two-center (2c) interaction between d metals or between a d metal and a p element, similarly to those reported for Sc−Ge, $(Sc-Sc)^{2+}$,[45,46] and Cu−Cu.[47] The basin of the ELI-D maximum located in the vicinity of the Au−Al1 contact is intersecting only the basins of these two atoms, thus indicating also here a 2c bonding. A similar topological situation is found for the Ir−Al1 interaction, which also has 2c character. The next type of ELI-D maxima is located close to the Al21−Al22 contacts and may suggest a direct Al−Al bonding. Nevertheless, intersection analysis reveals that the largest part of the basin for this attractor is located within the QTAIM atom of Ir and its basin has a contribution from Au, revealing the four-center (4c) bonding in this part of the crystal structure being in agreement with the relatively large Al−Al distance of 2.89 Å, which is compatible with the distance of 2.86 Å in elemental Al, where a picture of a multicenter interaction is often applied to understand the bonding. Even more complex topological situations are represented by the ELI-D between Al1 and Al21 as well as between Al1 and Al22, respectively. The according maxima are located close to the direct lines between the nuclei. Nevertheless, intersection analysis shows that in each case five atoms contribute to these interactions, both Al and three TM atoms, i.e., revealing the five-center (5c) bonding in this region of the crystal structure.

The character of the bonding attractors for the model with $z = 0.063$ is similar to that with $z = 0.0$. All two- and three-center (3c) interactions remain unchanged. One of the 5c interactions observed for $z = 0.0$ disappears for $z = 0.063$. The picture for $z = -0.063$ is more different. A new 2c bond Au−Al22 appears, and the former (4c) interaction now becomes a 3c one. This leads to a seven-coordinated Au atom counting only 2c bonds, which is remarkably different from the two other configurations, where each Au atom forms only four 2c bonds. Together with the largest energy for this model, this makes it less probable for the crystal structure of $Al_3AuIr$.

In the crystal structure of $Al_5Co_2$, the 2c and multicenter interactions are distributed in a way that allows for interpretation as 2c-bonded zero-dimensional clusters separated by the regions with multicenter bonds.[48] The 2c and multicenter interactions in $Al_3AuIr$ are distributed in layers perpendicular to the [001] direction (Figure 7, bottom); a similar topology of bond distribution was observed in $Al_{13}Co_4$.[49,50] Ir and Au atoms are interconnected via Al, forming puckered layers. The Au atoms on the outer side of such layers are additionally "protected" by 2c bonds to the Al21 atoms, whereby the Ir−Al22 interaction is mainly of multicenter character. The layers of 2c bonds are separated by 4c and 5c bonds. Assuming that the strength of the 2c bonds is larger than those for the multicenter bonds (this is known, for instance, for the B compounds), the region of 4c and 5c interactions is intuitively more suitable for cleaving of the material and formation of the more stable surface with Ir atoms on the outer side.

While stable decagonal quasicrystals exist in the same area of the Al−Cu−Co ternary system ($Al_{65}Cu_{20}Co_{15}$ and $Al_{65}Cu_{15}Co_{20}$[51]), complex metallic alloys remain to be found in the Al−Au−Ir phase diagram. Additional experimental works are ongoing to further investigate this ternary phase diagram.

## 4. CONCLUSION

A sample with nominal composition $Al_{65}Au_{20}Ir_{15}$ was prepared and annealed to 950 °C for 72 h. This sample contained almost exclusively a single ternary phase. Although this compound is formed at the same compositional region as the expected Al−TM−TM quasicrystalline phases,[2,4−6] analysis using single-crystal XRD combined with EDX measurements indicates a $Ni_2Al_3$ structure type with stoichiometry $Al_3AuIr$ and a narrow homogeneity range. This compound adopts the space group $P\bar{3}m1$ with the lattice parameters $a = 4.2584(5)$ Å and $c = 5.1991(7)$ Å. A model with a split position has been introduced to explain the unusually strong displacement anisotropy identified at the Al atom position in the origin. An isoelectronic substitution rule suggests a phase stabilized by a Hume−Rothery mechanism. Ab initio calculations demonstrate the presence of a pseudogap around $E_F$, and the calculated formation enthalpies indicate an enhanced stability for the $Al_3AuIr$ compound compared to the hypothetical $Al_6Au_3Ir$ phase. 2c and multicenter interactions have been identified in the $Al_3AuIr$ phase. Because of the layered distribution of these interactions, a preferential cleavage of the material is expected at puckered planes perpendicular to the [001] direction.

## ■ AUTHOR INFORMATION

### Corresponding Author

*E-mail: julian.ledieu@univ-lorraine.fr.

### Notes

The authors declare no competing financial interest.

## ■ ACKNOWLEDGMENTS

The INC−CNRS and the Région Lorraine are acknowledged for their financial support. This work is a result of the cooperation within the European C-MAC.

## ■ REFERENCES

(1) Tsai, A.; Inoue, A.; Masumoto, T. *Jpn. J. Appl. Phys.* **1988**, *27*, L1587−L1590.

(2) Katrych, S.; Weber, T.; Kobas, A.; Massueger, L.; Palatinus, L.; Chapuis, G.; Steurer, W. *J. Alloys Compd.* **2007**, *428*, 164−172.

(3) Athanasiou, N. *Int. J. Mod. Phys. B* **1997**, *11*, 2443−2464.

(4) Kapush, D.; Grushko, B.; Pavlyuchkov, D.; Velikanova, T. *Chem. Met. Alloys* **2009**, *2*, 30−33.

(5) Dshemuchadse, J.; Kuczera, P.; Steurer, W. *Intermetallics* **2013**, *32*, 337−343.

(6) 10th International Conference on Quasicrystals (ICQ10), ETH, Zurich, Switzerland, July 6−11, 2008. Oishi, A.; Nishimoto, K.; Tamura, R. *Zeitschrift für kristallographie* **2009**, *224*, 115−118.

(7) Okamoto, H. *J. Phase Equilib.* **1991**, *12*, 114−115.

(8) Okamoto, H. *J. Phase Equilib. Diffus.* **2009**, *30*, 206−207.

(9) Ferrin, P. A.; Kandoi, S.; Zhang, J.; Adzic, R.; Mavrikakis, M. *J. Phys. Chem. C* **2009**, *113*, 1411−1417.

(10) Okada, M.; Nakamura, M.; Moritani, K.; Kasai, T. *Surf. Sci.* **2003**, *523*, 218−230.

(11) Sheldrick, G. M. *Acta Crystallogr., Sect. A: Found. Crystallogr.* **2008**, *64*, 112−122.

(12) Akselrud, L.; Grin, Y. *J. Appl. Crystallogr.* **2014**, *47*, 803−805.

(13) Kresse, G.; Hafner, J. *Phys. Rev. B: Condens. Matter Mater. Phys.* **1993**, *47*, 558−561.

(14) Kresse, G.; Hafner, J. *Phys. Rev. B: Condens. Matter Mater. Phys.* **1994**, *49*, 14251−14269.

(15) Kresse, G.; Furthmüller, J. *Phys. Rev. B: Condens. Matter Mater. Phys.* **1996**, *54*, 11169−11186.

(16) Kresse, G.; Furthmüller, J. *Comput. Mater. Sci.* **1996**, *6*, 15−50.

(17) Blöchl, P. *Phys. Rev. B: Condens. Matter Mater. Phys.* **1994**, *50*, 17953−17979.

(18) Kresse, G.; Joubert, D. *Phys. Rev. B: Condens. Matter Mater. Phys.* **1999**, *59*, 1758−1775.

(19) Perdew, J. P.; Burke, K.; Ernzerhof, M. *Phys. Rev. Lett.* **1996**, *77*, 3865−3868.

(20) Perdew, J. P.; Burke, K.; Ernzerhof, M. *Phys. Rev. Lett.* **1997**, *78*, 1396−1396.

(21) Jepsen, O.; Burkhardt, A.; Andersen, K. *The Program TB-LMTO-ASA 4.7*; Max-Planck-Institut für Festkörperforschung: Stuttgart, Germany, 1999.

(22) von Barth, U.; Hedin, L. *J. Phys. C: Solid State Phys.* **1972**, *5*, 1629−1642.
(23) Andersen, O. *Phys. Rev. B* **1975**, *12*, 3060−3083.
(24) Lambrecht, W.; Andersen, O. *Phys. Rev. B: Condens. Matter Mater. Phys.* **1986**, *34*, 2439−2449.
(25) Kohout, M. *Faraday Discuss.* **2007**, *135*, 43−54.
(26) Bader, R. *Atoms in Molecules, A Quantum Theory*; Clarendon Press and Oxford University Press Inc.: New York, 1994.
(27) Raub, S.; Jansen, G. *Theor. Chem. Acc.* **2001**, *106*, 223−232.
(28) *Kohout04, DGrid*, version 4.6; Max Planck Institute: Leipzig, Germany, 2001.
(29) Voort, G. V. *Color Metallography, Metallography and Microstructures*; ASM Handbook Series; ASM International: Materials Park, OH, 2004; Vol. *9*.
(30) Selikson, B.; Longo, T. *Proc. IEEE* **1964**, *52*, 1638−1641.
(31) Puselj, M.; Schubert, K. *J. Less-Common Met.* **1974**, *35*, 259−266.
(32) Grin, Y.; Peters, K.; Burkhardt, U.; Gotzmann, K.; Ellner, M. Z. *Kristallogr.* **1997**, *212*, 439−444.
(33) Murray, J.; Okamoto, H.; Massalski, T. *Bull. Alloy Phase Diagrams* **1987**, *8*, 20−30.
(34) Ode, M.; Abe, T.; Murakami, H.; Yamabe-Mitarai, Y.; Hara, T.; Nagashio, K.; Kocer, C.; Onodera, H. *Intermetallics* **2008**, *16*, 1171−1178.
(35) Bradley, A. J.; Taylor, A. *Philosophical Magazine Series 7* **1937**, *23*, 1049−1067.
(36) Skolozdra, R. V.; Prevarskii, A. P.; Cherkashin, G. G. *Diagrammy Sostoyaniya Met. Sist.* **1971**, 167.
(37) Grushko, B.; Urban, K.; Freiburg, C. *Scr. Metall. Mater.* **1991**, *25*, 2533−2536.
(38) Sabiryanov, R.; Bose, S.; Burkov, S. *J. Phys.: Condens. Matter* **1995**, *7*, 5437−5459.
(39) Ellner, M.; Kattner, U.; Predel, B. *J. Less-Common Met.* **1982**, *87*, 305−325.
(40) Yurechko, M.; Fattah, A.; Velikanova, T.; Grushko, B. *J. Alloys Compd.* **2001**, *329*, 173−181.
(41) Massalski, T. B.; Mizutani, U. *Prog. Mater. Sci.* **1978**, *22*, 151−262.
(42) Trambly de Laissardière, G.; Nguyen-Manh, D.; Mayou, D. *Prog. Mater. Sci.* **2005**, *50*, 679−788.
(43) See http://gurka.fysik.uu.se/ESP/.
(44) Ortiz, C.; Eriksson, O.; Klintenberg, M. *Comput. Mater. Sci.* **2009**, *44*, 1042−1049.
(45) Kohout, M.; Wagner, F.; Grin, Y. *Theor. Chem. Acc.* **2002**, *108*, 150−156.
(46) Wagner, F.; Bezugly, V.; Kohout, M.; Grin, Y. *Chem. - Eur. J.* **2007**, *13*, 5724−5741.
(47) Grin, Y.; Wagner, F.; Armbrüster, M.; Kohout, M.; Leithe-Jasper, A.; Schwarz, U.; Wedig, U.; Georg von Schnering, H. *J. Solid State Chem.* **2006**, *179*, 1707−1719.
(48) Ormeci, A.; Grin, Y. *Isr. J. Chem.* **2011**, *51*, 1349−1354.
(49) Shin, H.; Pussi, K.; Gaudry, E.; Ledieu, J.; Fournée, V.; Alarcón Villaseca, S.; Dubois, J.-M.; Grin, Y.; Gille, P.; Moritz, W.; Diehl, R. *Phys. Rev. B: Condens. Matter Mater. Phys.* **2011**, *84*, 085411(11).
(50) Armbrüster, M.; Kovnir, K.; Grin, Y.; Schlögl, R. In *Complex Metallic Alloys: Fundamentals and Applications*; Dubois, J.-M., Belin-Ferré, E., Eds.; Wiley-VCH Verlag GmbH & Co.: Weinheim, Germany, 2011; pp 385−399.
(51) Kuo, K.; Zhang, Z. *Prog. Cryst. Growth Charact. Mater.* **1997**, *34*, 191−206.